Journal of Power Sources 543 (2022) 231823

Contents lists available at ScienceDirect

Journal of Power Sources

journal homepage: www.elsevier.com/locate/jpowsour

Glyme solvated Na and Li-ion capacitors based on *co*-intercalation process using pencil graphite as battery type electrode

Madhusoodhanan Lathika Divya [a], Yun-Sung Lee [b,**], Vanchiappan Aravindan [a,*]

[a] Department of Chemistry, Indian Institute of Science Education and Research (IISER), Tirupati, 517507, India
[b] School of Chemical Engineering, Chonnam National University, Gwang-ju, 61186, Republic of Korea

HIGHLIGHTS

- High-performance Li-ion and Na-ion capacitors are fabricated with pencil graphite.
- "Glyme" family solvents are used to enable solvent-co-intercalation.
- Usage of "Glyme" family solvents results in a trade-off between cell safety and energy.
- Max. energy density of 47 and 78.7 Wh kg^{-1} is noted for Li and Na-ion capacitors.

ARTICLE INFO

Keywords:
Glyme solvated Na and Li-ion capacitors
Co-intercalation
Solvated ion intercalation
Alkali metal ion hybrid supercapacitors
Pencil graphite
Kinetic mismatch

ABSTRACT

Co-intercalation, intercalation of solvated ions received significant research interest in the last decade mainly due to faster charge-discharge kinetics with enhanced diffusion and more excellent stability. Moreover, for the assembly of alkali metal-ion hybrid supercapacitors, with battery type anode and capacitive cathode, a co-intercalation-based anode is a suitable option to avoid the kinetic mismatch between the two electrodes and hence can guarantee better performance. In the present work, we considered pencil graphite (PG B), a cheap and readily available graphite silica composite, as a battery-type anode and commercial activated carbon (AC) as cathode for the assembly of glyme solvated Na and Li-ion capacitors ((PG B/1 M $NaCF_3SO_3$ in diglyme/AC) gs−NIC & ((PG B/1 M $LiPF_6$ in tetraglyme/AC) gs−LIC). Such device prototypes could exhibit maximum energy-power storage capability of 78.7 Wh kg^{-1} and 3.73 kW kg^{-1} for gs−NIC and 47 Wh kg^{-1} and 3.13 kW kg^{-1} for gs−LIC. Besides, the gs−NIC system with the minimum capacity and kinetic imbalance between the two electrodes displayed brilliant cyclic stability of >97% capacity retention after 6000 charge-discharge cycles at a current density of 1 A g^{-1}. However, the co-intercalation electrolyte system (salt and solvent) plays a vital role in the device's overall performance.

1. Introduction

Alkali metal-ion hybrid supercapacitors (AMIHSC) are emerging electrochemical energy storage devices, merging battery and capacitor types electrodes with alkali metal ion transport kinetics [1]. Lithium (Li) or sodium (Na) ion-based hybrid capacitors (Lithium-ion capacitors, LICs & sodium-ion capacitors, NICs) can store energy 4–5 times higher than conventional supercapacitor devices such as electric double-layer capacitors, EDLCs [2–4]. Generally, battery type electrode delivers a higher capacity than capacitor type electrode, whereas the latter provides improved stability and faster kinetics [5–8]. Thus, the energy and power density of the AMIHSC device is mainly restricted by capacitive and battery-type electrodes, respectively [1,9]. The charge-storage mechanism in battery-type electrodes is mostly reversible intercalation/de-intercalation of metal ions to/from the electrode and is also limited by diffusion kinetics of metal ions [10,11]. However, it is well established that the intercalation (redox reaction) is much slower than capacitive energy storage mechanisms such as adsorption/desorption of ions to the electric double layer of the capacitive electrode [12]. Integration of these two electrodes by minimizing the kinetic mismatch results in an ideal AMIHSC capable of storing more energy with high power capability [13,14]. Hybrid energy storage systems have

* Corresponding author.
** Corresponding author.
E-mail addresses: leeys@chonnam.ac.kr (Y.-S. Lee), aravind_van@yahoo.com (V. Aravindan).

https://doi.org/10.1016/j.jpowsour.2022.231823
Received 10 May 2022; Received in revised form 11 June 2022; Accepted 2 July 2022
Available online 20 July 2022

recently gained increasing research interest as they can become the core technology among electrochemical energy storage systems, even in electric vehicles in the immediate future [15].

Graphite, the state of art anode material with a conventional intercalation mechanism, is considered a suitable battery-type electrode (theoretical capacity of ~372 mAh g^{-1} with low reduction potential ~0.1 V *vs.* Li^+/Li) in LIC assembly [16–19]. However, it is unsuitable for NIC as robust local interactions between the graphene layers and Na^+ ions result in negligible Na storage capacity in graphite due to the instability of binary graphite intercalation compounds (*b*-GICs) [20]. In the last decade, researchers found that Na^+ can be reversibly stored with high capacity in graphite anode through the co-intercalation mechanism in which ternary GICs (*t*-GICs) are formed [21,22]. Previous studies also reported that co-intercalation results in better initial coloumbic efficiency (CE) with thinner and uniform solid electrolyte interface (SEI) layer formation. Moreover, improved kinetics in co-intercalation due to the fast diffusion of solvated ions can boost rate performance. Besides, co-intercalation could efficiently improve the pseudocapacitance contribution in the total charge storage mechanism. Because of the benefits of co-intercalation, it has been considered for different metal ions and studied the performance of batteries and hybrid capacitors with the co-intercalation-based anode. The studies reported that compared with conventional intercalation, co-intercalation-based electrodes provide improved kinetics with long-term stability for the device [23–25].

Pencil graphite (PG) electrodes as graphite silica composites have started gaining attention as active anode materials for Li-based energy storage systems due to their cost-effectiveness and electrochemical features [26–28]. This user-friendly electrode materials are readily available and are composed of graphite, silica in the form of clay, and wax in varying proportions which depend on the grading scale such as H (hardness) and B (darkness). The higher the number of H, the harder the pencil due to increased clay content, whereas the higher the number of B, darkness is improved due to significant graphite content. In this study, we have selected PG 1B grade material (~70% graphite, 25% clay & 5% wax) as electrode material for Na and Li-ion co-intercalation process using the glyme-based solvent. We also assembled and studied the performance of glyme solvated Na/Li metal-ion hybrid supercapacitors based on co-intercalation using Pencil graphite anode and activated carbon cathode.

2. Experimental section

2.1. Preparation of pencil graphite as active electrode material

Pencil grade 1B (PG B) of Kasimir drawing pencils was randomly selected as the electrode material. The wooden casing of the pencils was removed, and the lead was broken down into small pieces. Using a high-energy ball mill (SPEX, USA) with a 1:10 ball ratio, the lead pieces were milled for 5 min. Further, it was ground into fine powder in an agate mortar pestle and was directly used as anode active material for electrode preparation.

2.2. Physiochemical characterization of pencil graphite material

Powder X-ray diffraction, XRD (45 kV @ 200 mA using Cu- K_β filter and D/teX Ultra 250 detector), was performed within the 2θ range of 10–80° at a scan speed of 0.5° min^{-1} and 0.01° step. Raman spectrum of the PG B material was recorded with LabRam HR 800 UV Raman microscope (Horiba Jobin-Yvon, France) with 515 nm Diode laser as excitation light source and CCD detector within the wavelength range of 1000–3500 cm^{-1} at room temperature. The surface chemical composition of the material was analyzed using X-ray photoelectron spectroscopy (XPS) measurements. The morphology and elemental composition were investigated using Scanning electron micrograph (SEM) images and Energy-dispersive X-ray spectroscopy (EDS) data. The internal structure of the PG B material sample was observed under a transmission electron microscope (TEM) and high-resolution TEM (HR-TEM). The crystalline nature of the material was also analyzed from a selected area electron diffraction pattern (SAED) recorded using TEM. High angle annular dark-field (HAADF) images were recorded with SEM to obtain the atomic-level structure of the PG B material considered. Thermogravimetric analysis of the material sample was recorded with a DTG 60H thermal analyzer.

2.3. Electrode fabrication and cell assembly

The slurry was formed by mixing active material (PG B), conductive carbon (acetylene black), and polyvinylidene fluoride (PVdF) in the ratio of 80:10:10 using 1-methyl, 2-pyrrolidone (NMP) as solvent. The obtained homogeneous slurry mix was coated on Cu foil using doctor blade apparatus and then kept in a hot air oven for ~4 h. To yield a uniform coating, the slurry-coated foils were hard-pressed under a hot roll press (Tester Sangyo, Japan). 14 mm diameter PG B disc electrodes were punched out with an electrode cutter and were considered as the active electrode for anode half-cell and LIC assembly. Commercial activated carbon (AC, YP80F Kuraray, Japan), having a surface area of 2100 m^2 g^{-1} & pore volume of 0.97 mL g^{-1}, was considered as cathode active material. AC, acetylene black (conductive carbon), and teflonized acetylene black (TAB-2, binder) were mixed at an 80:10:10 ratio in an agate mortar and pestle using ethanol. The thin film of electrode material formed was pressed on a 14 mm diameter stainless steel mesh (Goodfellow, UK) current collector and considered as the active electrode for cathode half-cell and LIC assembly. In addition, slurry-coated Al electrodes were also used for half-cell performance analysis. Before cell assembly, fabricated electrodes (PG-B & AC) were kept in the vacuum chamber for ~4 h to ensure the proper drying of the electrodes. Co-intercalation of Na^+ and Li^+ ions in PG B material was analyzed in coin cells (CR 2016), assembled inside Ar filled glove box. Before the fabrication of hybrid capacitors, the solvated ion intercalation mechanism was studied in half-cell configurations made up of Na or Li metal as counter/reference electrodes. 1 M sodium trifluoromethanesulfonate ($NaCF_3SO_3$, 98% Sigma Aldrich) in diglyme or bis(2-methoxyethyl) ether solvent was used as an electrolyte for Na^+ ion co-intercalation. At the same time, 1 M lithium hexafluorophosphate ($LiPF_6$) in tetraglyme (tetraethylene glycol dimethyl ether) was used as an electrolyte for Li^+ ion co-intercalation. Both PG B anode half-cells and AC cathode half-cells were made with these electrolytes and Whatman paper (1825–047, GF/F) as separators in the coin cell assembly. Glyme solvated Na and Li metal-ion capacitors were assembled by coupling presodiated/prelithiated PG B electrode with AC cathode of balanced mass using the same electrolyte separator system.

2.4. Electrochemical characterization

Voltage profiles or galvanostatic charge-discharge (GCD) analysis, Cyclic voltammetric profiles (CV), and Electrochemical Impedance Spectroscopy (EIS) studies of the assembled coin-cells were executed with the help of a Battery tester, BCS 805 (Biologic, France). Na/PG B and Na/AC half-cells were tested within the potential window of 0.005–2.5 V and 1.5–4.2 V *vs.* Na^+/Na, respectively. Similarly, Li/PG B and Li/AC half-cells were tested within the potential window of 0.05–2.5 V and 1.5–4.2 V *vs.* Li^+/Li, respectively. The voltage window of the assembled glyme solvated Na/Li metal-ion capacitors (gs−NIC & gs−LIC) were limited to 1.0–3.7 V and 1.3–3.8 V, respectively, by considering their co-intercalation potential in the anode half-cells. The energy and power density values of the assembled AMIHSCs were calculated based on the total mass of active material present on both anode and cathode.

3. Results and discussion

3.1. Material characterization

The Powder X-ray diffraction (XRD) pattern of PG B material, Fig. 1 (a), shows two prominent peaks at 26.62 & 54.72° corresponding to (002) and (004) planes of natural graphite. The peaks also contribute to (101) & (202) planes of the Quartz phase representing the clay component. In addition, all the peaks of standard graphite (00-023-0064 with space group 194: P63/mmc) and some peaks of the standard SiO_2 phase (01-083-0539 with space group 152: P3121) can be noticed in the XRD pattern recorded, that indicates the graphite clay composite nature of the PG B material [26]. The Raman spectrum in Fig. 1(b) shows three characteristic peaks of carbon materials positioned at 1350, 1578, and 2710 cm^{-1}, corresponding to the defect band (D-band), the band of graphite (G-band), and 2D band (G* band) [29]. D band represents defects or disorder in the graphitic lattice that arises due to the in-plane breathing mode associated with the graphitic structure. A less intense D-band indicates there is not as much disorder in the PG B material. G band results from in-plane tangential vibration of C–C bonds (sp^2 bonded carbon atoms), E_{2g} mode in the graphitic structure. The 2D band (D overtone or second order of D band) or G* band is due to the second-order phonon process, and it has strong frequency dependence on the excitation source energy. 2D band and G band together represent Raman signature of graphitic sp^2 materials [30]. While considering the area under the peaks, the PG B material exhibit an I_D/I_G value and I_{2D}/I_G value of 0.16 and 1.6, respectively, indicating few graphitic layer material with low defect intensity [31,32]. Fig. S1 illustrates the raw XPS spectrum of the PG B material, which can be used to determine the surface elemental compositions [33–35]. The survey spectrum shows the presence of carbon (86.09%), oxygen (13.91%), and a trace amount of silicon on the material surface. Si may originate from the clay (SiO_2) or binder component of the PG B material. Deconvoluted C1s and O1s spectrum is given in Fig. 1(c)& (d). High-resolution C1s spectra indicate that the material contains a substantial amount of sp^2 carbon (51.75%), 24.01% C–OH bonds, and 6.5% C═O bonds. The deconvoluted O1s spectra have three peaks corresponding to C═O (3.77%), C–OH (8.19%), and COOH (5.72%) surface functionalities. The presence of oxygen may be due to adventitious contamination or oxidation of the sample exposed to the atmosphere [36].

Fig. 2(a) presents the scanning electron microscopy (SEM) image of PG B lead powder material. The picture shows discrete flaky morphology of the material with heterogeneity, which develops due to foldings, cracks, and cavities on the surface. Transmission electron microscopy (TEM) image, Fig. 2(b) shows flat, thin sheets like crystallites formed by many graphene layers with a few dark colour shades on the surface corresponding to the clay/wax component of the PG B along with graphite. The high-resolution transmission electron microscope (HR-TEM) image in Fig. 2(c) displays lateral fringes, agreeing to an interlayer spacing of 3.3 Å, which can be credited to the (002) plane of graphite or (101) plane of the Quartz phase of the material. The SAED image in the inset of Fig. 2(c) demonstrates clear, bright diffraction spots with six-fold/hexagonal symmetry, representing crystalline graphite with a small degree of polycrystallinity induced by the clay component.

Energy dispersive spectroscopy (EDS) data in Fig. S2 illustrates the presence of aluminum and silicon (which may be present in the binder component) along with carbon and oxygen in the PG B material sample. But, the presence of Al may be attributed to sampling stubs in the SEM analyzer, as they are made of aluminum. In addition, the spectrum shows that ~75 wt.% of the total sample weight is constituted by carbon, indicating ~75% of graphite and ~25% of the clay binder component in the PG B material. Fig. 2 (d, e & f) shows the High-angle annular dark field image (HAADF) and the elemental mapping images of the PG B material. Elemental mapping shows uniform distribution of carbon and oxygen, whereas the presence of silicon is not shown as it appears to be present deeper within the PG material sample. The TGA plot presented in Fig. S3 shows that the material exhibited a two-stage decomposition pattern with corresponding peaks at 292 and 706 °C. The first decomposition before 400 °C represents the degradation of low molecular weight volatile polymer components (wax/binder composition) present in the sample. Weight loss above 500 °C pointing to the decomposition of the graphitic content of the material. The residue left (~27 wt.%) after 800 °C indicates thermally stable clay content or non-carbon content present in the PG B material.

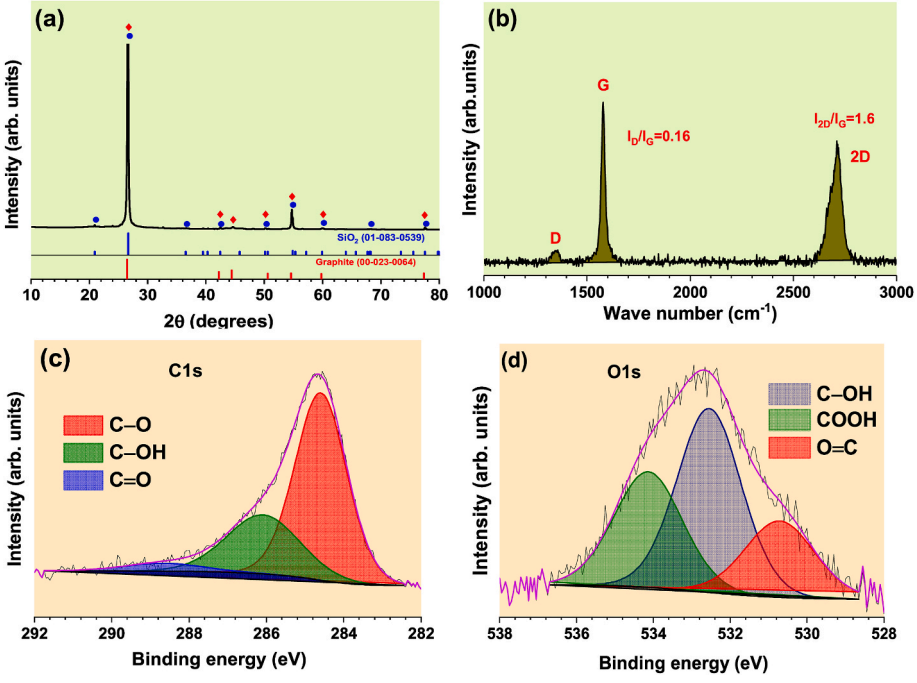

Fig. 1. (a) XRD pattern, (b) Raman spectra, (c) deconvoluted XPS of C1s, and (d) deconvoluted XPS of O1s of PG B material.

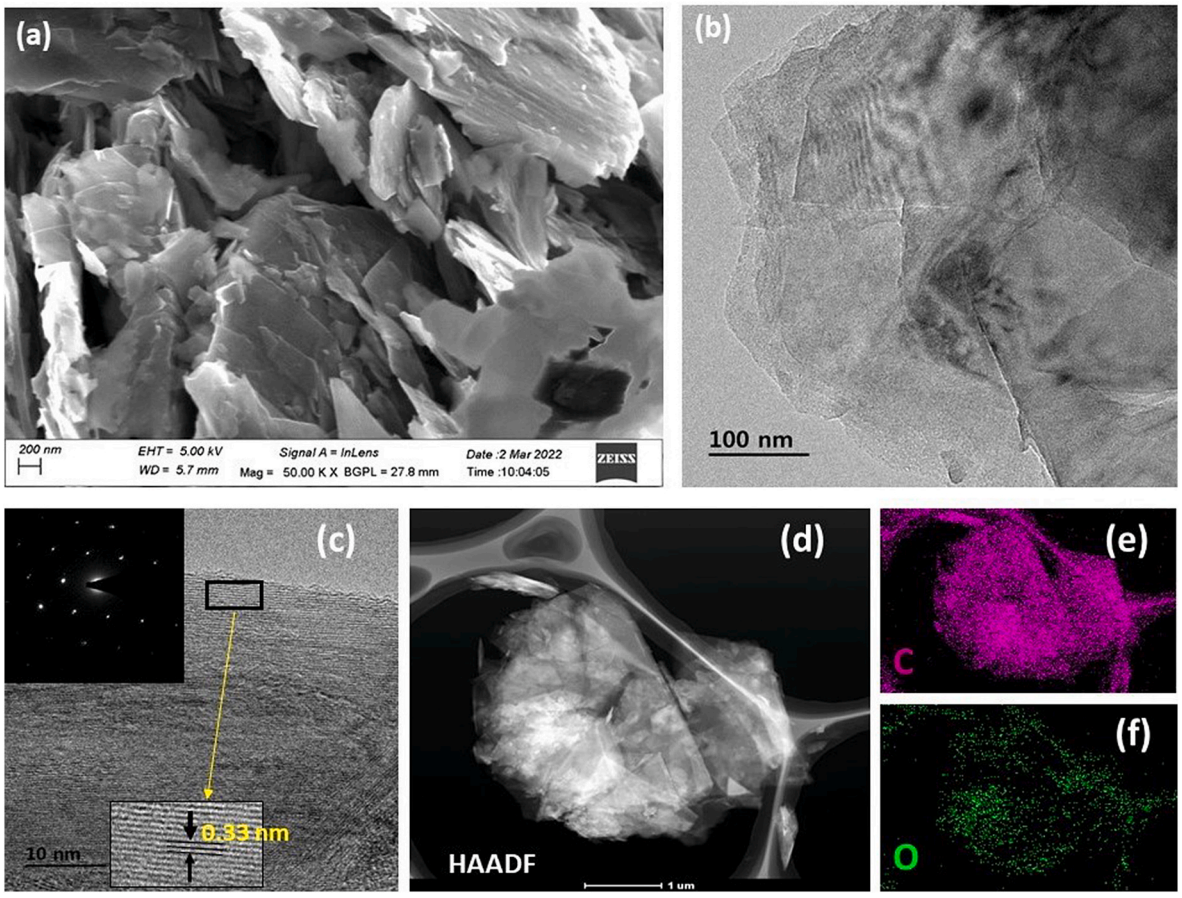

Fig. 2. (a) SEM, (b) TEM, (c) HR-TEM (SAED pattern at the inset), (d) HAADF, and (e) & (f) Corresponding elemental mapping images of PG B material.

3.2. Electrochemical performance

3.2.1. Glyme solvated Na metal ion hybrid supercapacitor, gs−NIC

The intercalation mechanism of glyme solvated Na metal ion into PG B electrode material was studied in half-cell assembly using 1 M $NaCF_3SO_3$ (NaOTf) in diglyme (G_2) as electrolyte. G_2 was selected as the solvent as it can exhibit better performance in graphite than other glyme-based solvents [37]. Besides, NaOTf was reported as the most suitable conductive salt in diglyme for Na-based graphitic cells [38]. The assembled half-cells with PG B electrode mass loading of ~1–1.5 mg cm^{-2} exhibited an initial open-circuit voltage (OCV) of ~2.0–2.5 V *vs.* Na^+/Na. The electrochemical performance of the half-cell was tested within the potential window of 0.005–2.5 V *vs.* Na^+/Na. Fig. 3(a) shows the GCD profile at current input of 100 mA g^{-1} and is comparable to previously reported studies on Na co-intercalation in graphitic materials [39–41]. The discharge profile comprises one sloping plateau (~0.97–0.6 V *vs.* Na^+/Na) and one flat plateau (~0.6–0.59 V *vs.* Na^+/Na), whereas the charge profile has two main sloping plateaus. The cells exhibited initial discharge–charge capacities of ~225 & 108 mAh g^{-1} with initial CE of 48%. Poor CE may be due to the initial activation of electrode material and solid electrolyte interface (SEI) formation associated with electrolyte decomposition. However, the GCD profile subsequently remains similar, and the cell could deliver improved coulombic efficiency (CE >97%) with second discharge charge capacities of ~114 & 111 mAh g^{-1}. We also tested the rate performance at different current density values ranging from 0.05 to 1.5 A g^{-1}, Fig. 3(b). We could notice that a minimum of 100 mA g^{-1} is required for effective co-intercalation, as there is no rise in discharge capacity value at a current density of 50 mA g^{-1} in comparison with the 100 mA g^{-1} discharge profile. Even at a high current of 1.5 A g^{-1}, the cells could deliver a discharge capacity of ~72 mAh g^{-1} with >99.99% CE. Fig. S4 (a) shows the GCD profile at different current density values. We could observe that rise in current density results in a fall in reduction potential (Na co-intercalation potential) and a rise in charge-discharge intersecting potential. After the rate performance analysis, the cell was continuously cycled at a current density of 1.0 A g^{-1}, and at the end of the 185th cycle, Na/PG B half-cell could retain a capacity of ~67 mAh g^{-1}, Fig. 3(c). Further, the cyclic stability of the fresh cell was tested at a current density of 0.1 A g^{-1}, which resulted in capacity retention of ~63% of the second discharge capacity after 100 GCD cycles. CE was less in the initial cycle, but a gradual increase to 100% could be observed during cycling Fig. S4(b).

In addition, the electrochemical property of this material was also analyzed by cyclic voltammogram (CV). Fig. 3(d) illustrates the CV profile of the first three cycles at a scan rate of 0.1 mV s^{-1}. The current profile in the first cycle (with broadened reduction peak) is different from the remaining cycles, as the material is undergoing activation during co-intercalation by the expansion of graphene layers [42]. This may also be due to the formation of the thin SEI layer mainly from the decomposition of the electrolyte. From the second cycle onwards, the prominent cathodic and anodic peaks were observed at 0.6–0.5 and 0.7–1.2 V *vs.* Na^+/Na, respectively. Fig. S5(a) shows the 3rd cycle CV profile at different scan rates ranging from 0.1 to 1 mV s^{-1}. As the scan rate increases, the peak current slowly rises, and the separation potential between reduction and oxidation peak gradually increases. This indicates minor polarization of the PG B electrode during sodiation and de-sodiation. The diffusivity of diglyme solvated Na^+ ion within the PG B material was determined by the Randles-Sevcik equation. Fig. S5(b) shows plots of linear fit between peak current and the square root of scan rate. The diffusion coefficient (D_{Na}) values for cathodic and anodic peaks were calculated as 7.57 × 10^{-7} and 3.08 × 10^{-7} cm^2 s^{-1}, respectively, which are in a slightly higher range in comparison with the D_{Na} value of

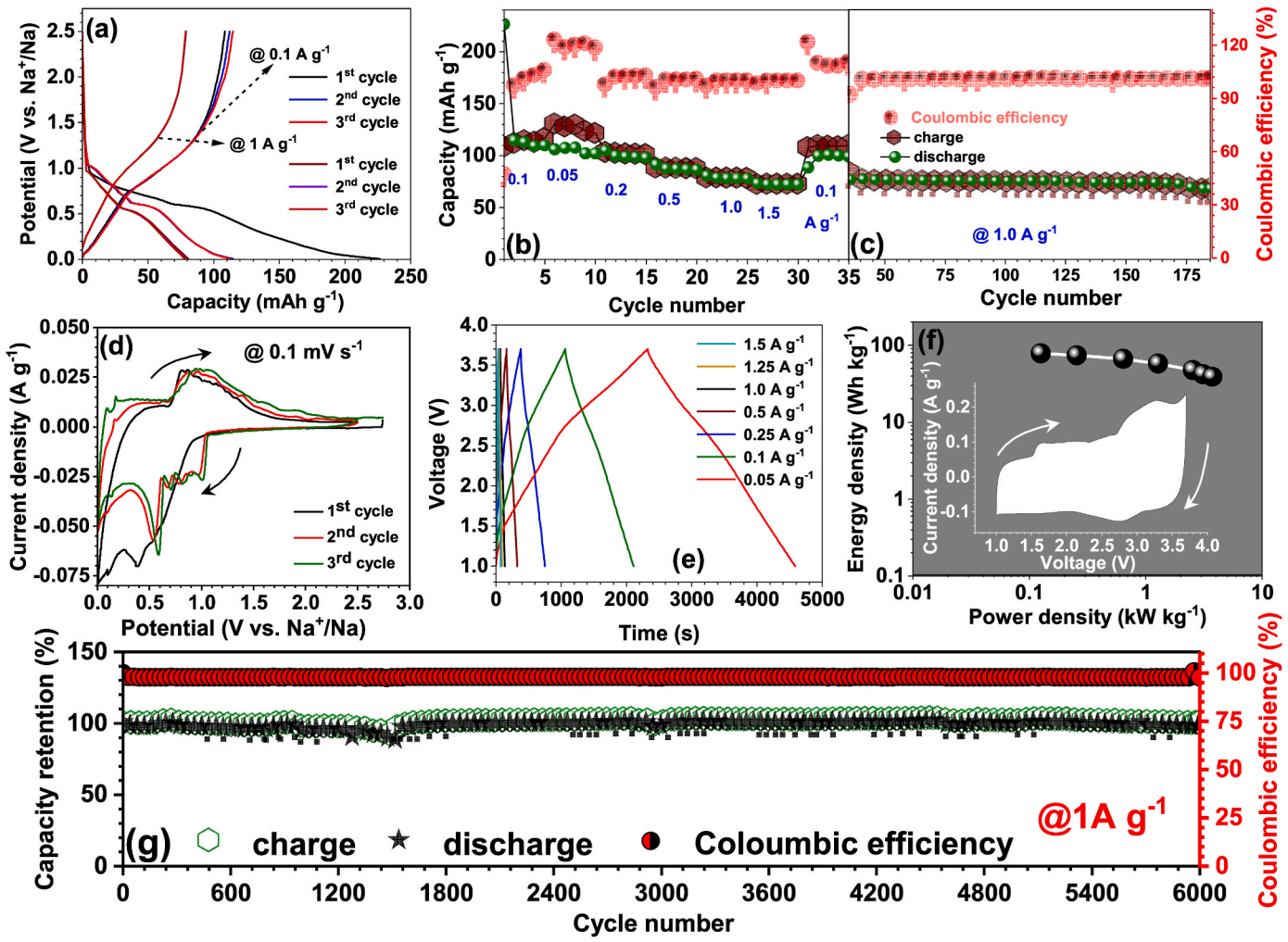

Fig. 3. Electrochemical performance of PG B material in Na-based half-cell and gs−NIC assembly with 1M CF_3SO_3Na in diglyme as the electrolyte: (a) GCD profile of Na/PG B half-cell, (b) Rate performance of Na/PG B half-cell, (c) Cyclic stability of Na/PG B half-cell at the current density of 1.0 A g^{-1}, (d) CV profile of Na/PG B half-cell at a scan rate of 0.1 mV s^{-1}, (e) GCD profile of PG B//AC-based gs−NIC at different current rates, (f) Ragone plot based on the total mass of active material in anode and cathode; inset: CV profile of PG B//AC gs−NIC at a scan rate of 1 mV s^{-1}, and (g) Cyclic stability of PG B//AC-based gs−NIC at a current density of 1 A g^{-1}.

previously studied graphitic materials [24,41]. Besides, the same CV curves with small voltage deviation at different scan rates point to boosted diffusion kinetics. According to the Randles-Sevcik equation, the relationship between scan rate (ν) and current response (i_p) can be expressed using the power law equation, $i_p = a\nu^b$ Where a & b are adjustable parameters. Fig. S5(c) provides plots fitting log (i_p) and log(ν), and corresponding b values were determined to be 0.75 and 0.9, respectively, for cathodic and anodic peaks. These b values indicate that electrochemical reaction-based charge storage comprises both capacitive contribution (pseudocapacitive/surface faradaic reactions) and diffusion-controlled faradaic reaction with a major contribution from the former. Surface capacitive contribution and diffusion-limited solvated Na^+ ion intercalation of electrode material were determined according to Dunn's method; which describes the total current (i_p) as the sum of capacitive current ($k_1\nu$) and diffusion-controlled current ($k_2\nu^{1/2}$) at any given potential (V). From the plot between $i_p/\nu^{1/2}$ and $\nu^{1/2}$, Fig. S5 (d), the value of k_1 and k_2 are obtained as 0.579 and 0.38 for the cathodic peak and 0.491 and 0.067 for the anodic peak, respectively. Fig. S5(e) shows the capacitive contribution at different scan rates, and the values indicate that it increases from 43% @ 0.1 mV s^{-1} to 70.73% at a scan rate of 1 mV s^{-1} [43].

Fig. S5(f) displays the electrochemical impedance spectroscopy (EIS) Nyquist plot of fresh Na/PG B half-cells within the frequency range of 10 kHz to 1 Hz. The equivalent circuit model given in the inset was used to fit the data. R_1 represents solution resistance, the combination of R_2 and R_3 gives the charge transfer resistance, Q_2 indicates constant phase element corresponding to surface film resistance and C_3 corresponds to double-layer capacitance. W denotes Warburg impedance in the given circuit. Thus, the cell exhibits R_1, R_2, and R_3 of 45.3, 157.5 and 154.5 Ω, respectively pointing to a kinetically facile system. The electrochemical behavior of AC-based cathode half-cell was tested using the same electrolyte system within the potential window of 1.5–4.2 V *vs.* Na^+/Na. The assembled Na/AC half-cells showed an OCV of 3.0–3.5 V *vs.* Na^+/Na. Fig. S6(a) shows the GCD profile for the first three cycles at a current density of 100 mA g^{-1}, which indicates a discharge capacity of ~71 mAh g^{-1} in the first discharge. The cyclic stability of Na/AC half-cells was tested, and we observed that the cell retains the same capacity even after 80 cycles with a CE of 92–93% Fig. S6(b). Glyme solvated Na-ion hybrid capacitor (PG B//AC, gs-NIC) was devised using a pre-sodiated PG B electrode as anode and AC electrode with balanced mass as the cathode (cathode to anode mass ratio is 1.5). Preisodiation can take away the effect of the first cycle irreversibility, and also this will guarantee the maximum working voltage window to the device. Being an electrolyte-consuming mechanism, co-intercalation-based charge storage in gs-NIC

with PG B anode can be explained with the following equations.

Electrolyte: $NaCF_3SO_3 \leftrightarrows CF_3SO_3^- + Na^+$ (1)

Anode half cell: PG B|1 M $NaCF_3SO_3$ in G_2|Na

$Negative\ \ electrode:\ Na + [G_2]_n \rightleftarrows Na^+(G_2)_n + e^-$ (2)

$Positive\ \ electrode:\ Na^+(G_2)_n + x\ PG\ B + e^- \leftrightarrows Na(G_2)_n PG\ B_x$ (3)

Cathode half-cell: AC|1 M $NaCF_3SO_3$ in G_2|Na

$Negative\ \ electrode:\ Na + [G_2]_n \rightleftarrows Na^+(G_2)_n + e^-$ (4)

$Positive\ \ electrode:\ AC + xCF_3SO_3^- - \leftrightarrows AC[CF_3SO_3]_x + xe^-$ (5)

gs-NIC:

$Anode:\ x\ PG\ B + Na^+(G_2)_n + e^- \leftrightarrows Na(G_2)_n PG\ B_x$ (6)

$Cathode:\ AC + xCF_3SO_3^- \leftrightarrows AC\left[CF_3SO_3^-\right]_x + xe^-$ (7)

Where '*n*' and '*x*' represent the number of solvent molecules co-intercalated per Na^+ ion and PG B atom, respectively; (n = 1 or 2; x = 16–26 from literature) [44]. During charging of the gs-NIC device, Na^+, and $CF_3SO_3^-$ ions are formed in the electrolyte, and there is solvation of Na^+ ions with G_2. $CF_3SO_3^-$ ions are accumulated on the AC cathode-electrolyte interface (adsorption), while G_2 solvated Na^+ ions ($Na^+(G_2)_n$) intercalate into PG B anode. During discharge, $CF_3SO_3^-$ ions and $Na^+(G_2)_n$ ions move away from AC cathode (desorption) and PG B anode (de-intercalation), respectively. The electrochemical performance of gs-NIC was tested within the voltage window of 1.0–3.7 V by considering the cathode potential window and also Na co-intercalation potential in the PG B anode. Fig. 3(e) shows the GCD profile at different current rates; a slight deviation from linearity during the charging and discharging profile indicates the presence of a hybrid (combination of faradaic and non-faradaic) charge storage mechanism. Fig. 3(f) illustrates the Ragone plot, showing promising energy (maximum 78.7 Wh kg^{-1} @ 125 W kg^{-1}) power (maximum 3.73 kW kg^{-1}@ 38.95 Wh kg^{-1}) storage capability of the device (obtained based on the total mass of active material present in both anode and cathode). At the inset CV profile of PG, B//AC based gs-NIC is given, quasi rectangular shape with increasing area from the scan rate of 1–5 mV s^{-1} and without any disturbances, Fig. S7(a) indicates a hybrid energy storage device with a good rate capability. Moreover, this device prototype demonstrated excellent cyclic stability of ~97% capacity retention even after 6000 charge-discharge cycles at a current density of 1 A g^{-1} with >99.9% CE Fig. 3(g). Fig. S7(b) provides the EIS Nyquist plot of fresh as well as cycled gs-NIC cells. Low values of R_s and R_{ct} with Warburg tail points to a kinetically balanced system with better charge storage capability and stability.

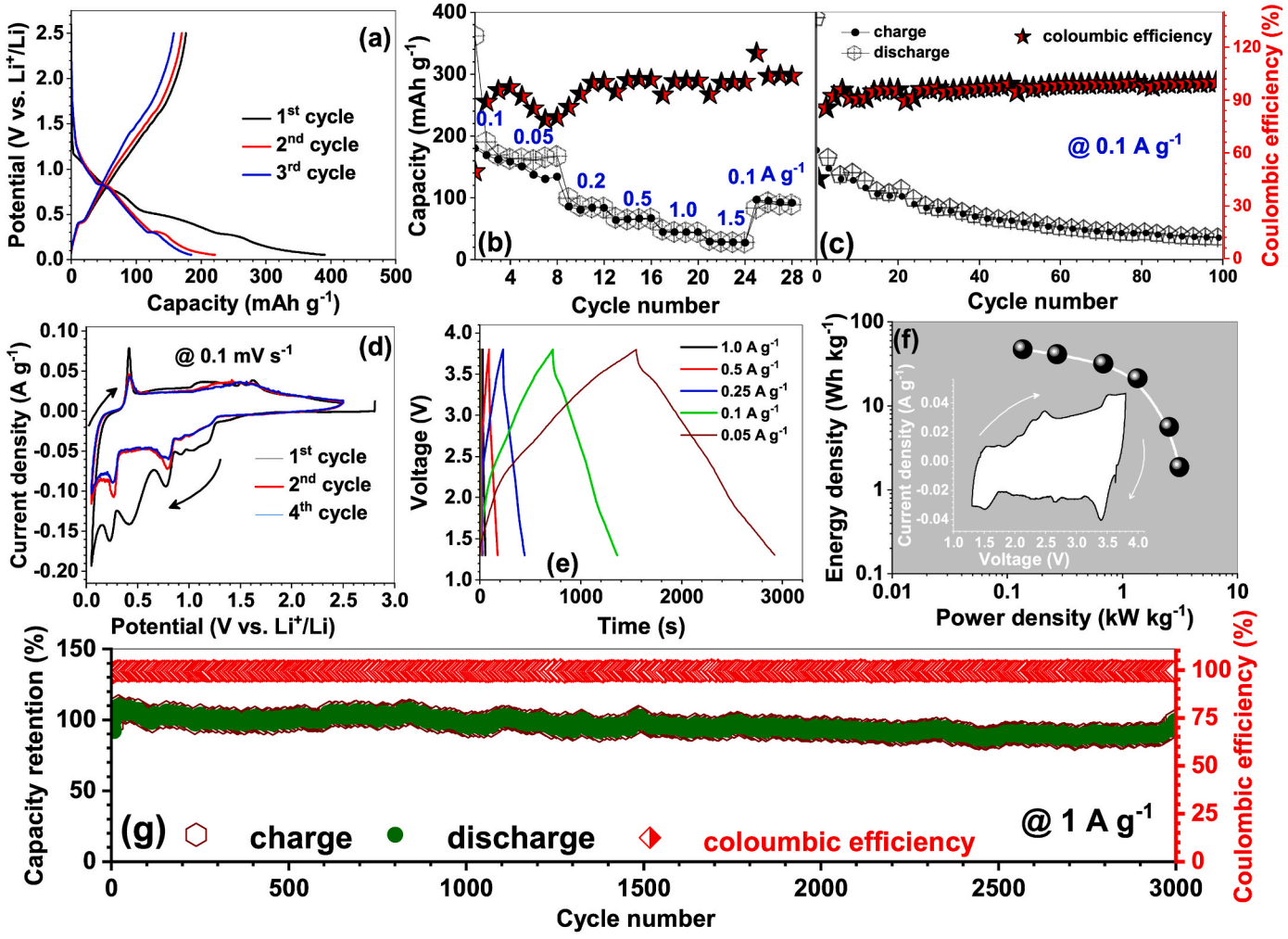

Fig. 4. Electrochemical performance of PG B material in Li-based half-cell and gs−LIC assembly with 1M $LiPF_6$ in tetraglyme as the electrolyte: (a) GCD profile of Li/PG B half-cell at a current density of 0.1 A g^{-1} (b) Rate performance of Li/PG B half-cell; (c) Cyclic stability of Li/PG B half-cell at a current density of 0.1 A g^{-1}; (d) CV profile of Li/PG B half-cell at 0.1 mV s^{-1}; (e) GCD profile of PG B//AC gs−LIC at different current rates; (f) Ragone plot based on the total mass of active material in anode and cathode, inset: CV profile of PG B//AC gs−LIC at a scan rate of 1 mV s^{-1}; (g) Cyclic stability of PG B//AC gs−LIC at a current density of 1 A g^{-1}.

3.2.2. Glyme solvated Li metal ion hybrid supercapacitor

Glyme solvated Li metal ion insertion into graphitic material differs from conventional intercalation of bare Li-ions. PG B electrode in the presence of 1 M $LiPF_6$ in TEGDME (G_4) with Li metal counter electrode was considered as anode half-cell. $LiPF_6$, the most commonly used salt for Li-based systems [45], generally exhibits poor solubility in glymes; G_4 can solubilize twice the salt concentration than G_2 [46]. Moreover, G_4 displays a slightly lower insertion potential for Li in graphite than other glymes [37]. The half-cell assemblies displayed an OCV of ~3.0–3.1 V *vs.* Li^+/Li. Fig. 4 presents the electrochemical behavior of the PG B electrode in Li-based half-cell and gs-LIC assembly. GCD and CV analysis of co-intercalation-based PG B electrode half-cells were studied within the potential window of 0.05–2.5 V *vs.* Li^+/Li. The GCD profile at a current density of 100 mA g^{-1}, Fig. 4(a). It was observed that the CE value was gradually increasing with cycle number such that 76.48% for the 2nd cycle, 86.7% for the third cycle, and ~99% for the 100th cycle. The discharge-charge capacity values were higher than that of Na co-intercalation, with first, second, and third discharge capacity values of 383, 220, and 181 mAh g^{-1}, respectively. The rate performance was analyzed at different current input values ranging from the current density of 0.05–1.5 A g^{-1}, and we observed that there is a fall in capacity with an increase in current density values where the performance at a current density of 0.05 A g^{-1} after 0.1 A g^{-1} was poor with low CE Fig. 4 (b). The cyclic stability of the cell was also tested at a current density of 0.1 A g^{-1}; the cell showed a discharge capacity of 36 mAh g^{-1} at the end of 100 cycles, Fig. 4(c). The figure shows the instability of the Li co-intercalation system in comparison with Na co-intercalation. Fig. 4 (d) displays the 1st, 2nd, and 4th cycle CV profile at a scan rate of 0.1 mV s^{-1}. The first cycle CV profile is different from subsequent cycles due to the initial activation of electrode material and or SEI layer formation, cause of initial irreversibility. The CV profiles agree with GCD profiles, such that in the first discharge, three flat plateaus correspond to 3 peaks in the CV profile at 0.77, 0.43, and 0.21 V *vs.* Li^+/Li. From the second cycle onwards, two plateaus at 0.79 and 0.27 V *vs.* Li^+/Li correspond to two peaks in the CV profile. However, for the charge profile, a similar pattern is observed for all the cycles with one flat plateau at ~0.4 V *vs.* Li^+/Li matching with a sharp peak in the CV profile and a sloping plateau between 1.2 and 1.74 V *vs.* Li^+/Li, indicating a broad peak in the CV profile attributed to the stepwise de-intercalation mechanism.

Fig. S8(a) shows the typical third cycle CV profile for various scan rates; it is observed that response current rises with an increase in scan rate, with a gradual decrease in cathode peak potential and an increase in anodic peak potential representing diffusion-controlled kinetics of charge storage mechanism. Whereas the peak at ~0.2–0.3 V *vs.* Li^+/Li in the cathodic scan disappeared for scan rates except for the scan rate of 0.1 mV s^{-1}. Fig. S8(b) describes the relationship between response current (i_p) and the square root of scan rate ($\sqrt{\nu}$) for cathodic-anodic peak pair at 0.6–0.8 and 1.2–1.74 V *vs.* Li^+/Li, respectively. According to the Randles- Sevcik equation, the D_{Li} value was calculated as 3.2 × 10^{-8} and 3.4 × 10^{-8} cm^2 s^{-1}, respectively, for cathodic and anodic reactions. Slightly distorted CV profiles at various scan rates point to less rate capability of PG B electrode for Li co-intercalation in comparison with Na co-intercalation process. In addition, the obtained *b* values of 0.35 and 0.53 for cathodic and anodic peaks indicate the absence of pseudocapacitance contribution in the total charge storage mechanism, Fig. S8(c). This may be due to the bulky size of tetraglyme solvated Li^+ ions in comparison with diglyme solvated Na^+ ions. Fig. S8(d) provides the EIS Nyquist plot before and after cycling of Li/PG B half-cell. Increased solution resistance and charge transfer resistance after cycling shows the poor kinetics of solvated Li-ion-based charge storage in PG B.

We also assembled a gs-LIC using prelithiated PG B as anode AC as the cathode in the same electrolyte system (G_4). Prior to that, the performance of AC was studied in half-cell assembly with Li metal counter electrode. Figs. S9(a) and (b) show the GCD profile and cyclic stability of Li/AC half-cell within the potential window of 1.5–4.2 V *vs.* Li^+/Li. The cell exhibited a 1st discharge capacity value of ~73 mAh g^{-1}. However, second cycle onwards, the cell demonstrated CE values ranging between 105 and 98%. Moreover, the cell delivered cyclic stability of ~79% capacity retention after 100 GCD cycles. We observed that replacing the stainless-steel current collector with Al-foil could provide much more stable performance for this electrolyte system. A cathode to anode mass ratio of three (cathode mass/anode mass = 2.5) was used for the assembly of gs-LICs. The working mechanism of gs-LIC is similar to that of gs-NIC in which G_2 solvent and $CF_3SO_3^-$ ions in Na-based electrolyte system are replaced with G_4 and PF_6^- ions in Li-based electrolyte. Fig. 4 (e) shows the near-linear GCD profile of the LIC device for various current rates (0.05–1.5 A g^{-1}), illustrating the combination of battery type and EDLC type charge storage mechanisms. The figure illustrates that an increase in the current rate results in fast charging and discharging of the LIC device. The Ragone plot given in Fig. 4(f) provides energy and power density values at different current rates, which are calculated based on the active mass on PG B and AC electrodes. The device prototype could deliver maximum energy-power density values of 47 Wh kg^{-1} and 3.13 kW kg^{-1} within the current tested rates. The CV profile of the device at a scan rate of 1 mV s^{-1}, given at the inset, shows a pseudo rectangular shape (small peaks corresponding to battery type reactions along with EDLC mechanism). Further, the cyclic stability of the gs-LIC system was found to be ~97% capacity retention after 3000 GCD cycles at a current density of 1 A g^{-1}) with >99.9% CE for all the cycles, Fig. 4(g). Fig. S10 shows the EIS Nyquist plot of this LIC assembly before and after cycling. Low values of R_s and R_{ct} after cycling in comparison with the corresponding values of fresh LIC point to a stable LIC system irrespective of issues associated with half-cell performance.

3.3. Performance analysis and comparison

The observed difference between the co-intercalation-based energy storage mechanism of Na and Li-based systems include.

i. Change in co-intercalation potential; such that a strong cathodic peak at 0.5–0.6 V *vs.* Na^+/Na was observed for Na-based half-cell, whereas a two-step mechanism with medium intensity peaks at 0.7 and 0.1 V *vs.* Li^+/Li was observed for Li based systems.
ii. Li-based systems showed higher specific capacity in comparison with Na-based systems within the tested potential window.
iii. However, Na-based cells exhibited better cycle life and rate capability. The main reason for the capacity fade in Li based system may be due to the competitive formation of binary-GICs along with ternary-GICs, which are not stable in the case of Na.
iv. The presence of pseudocapacitive charge storage is observed for Na-based systems. However, Li-based systems exhibited a complete battery-type mechanism.

Fig. 5 illustrates the comparison of the performance of gs-NIC and gs-LIC assembled. The main obstacle in the assembly and real-world application of AMIHSCs is the imbalance in the capacity values and kinetics of both battery type anode and capacitive type cathode. Low range capacity values of capacitive cathodes can be overcome by considering a suitable mass ratio between anode and cathode to balance the charge. At the same time, sluggish cation diffusion in battery type anode results in a kinetic imbalance between the two electrodes. Achieving an optimum mass balance between anode and cathode is tremendously challenging. Thus it is necessary to find a suitable anode and cathode with a decent kinetic match, which can result in nearly equal electrode mass (minimum mass ratio) and hence the assembly of a perfect AMIHSC device. Fig. 5(a &b) display the GCD profile of both half-cells and hybrid capacitors at a current density of 0.1 A g^{-1}, explaining the kinetic balance in the gs-NIC system (mass ratio, cathode/anode = 1.5) in comparison with gs-LIC (mass ratio, cathode/anode = 2.5) system; which elucidate the superior performance of

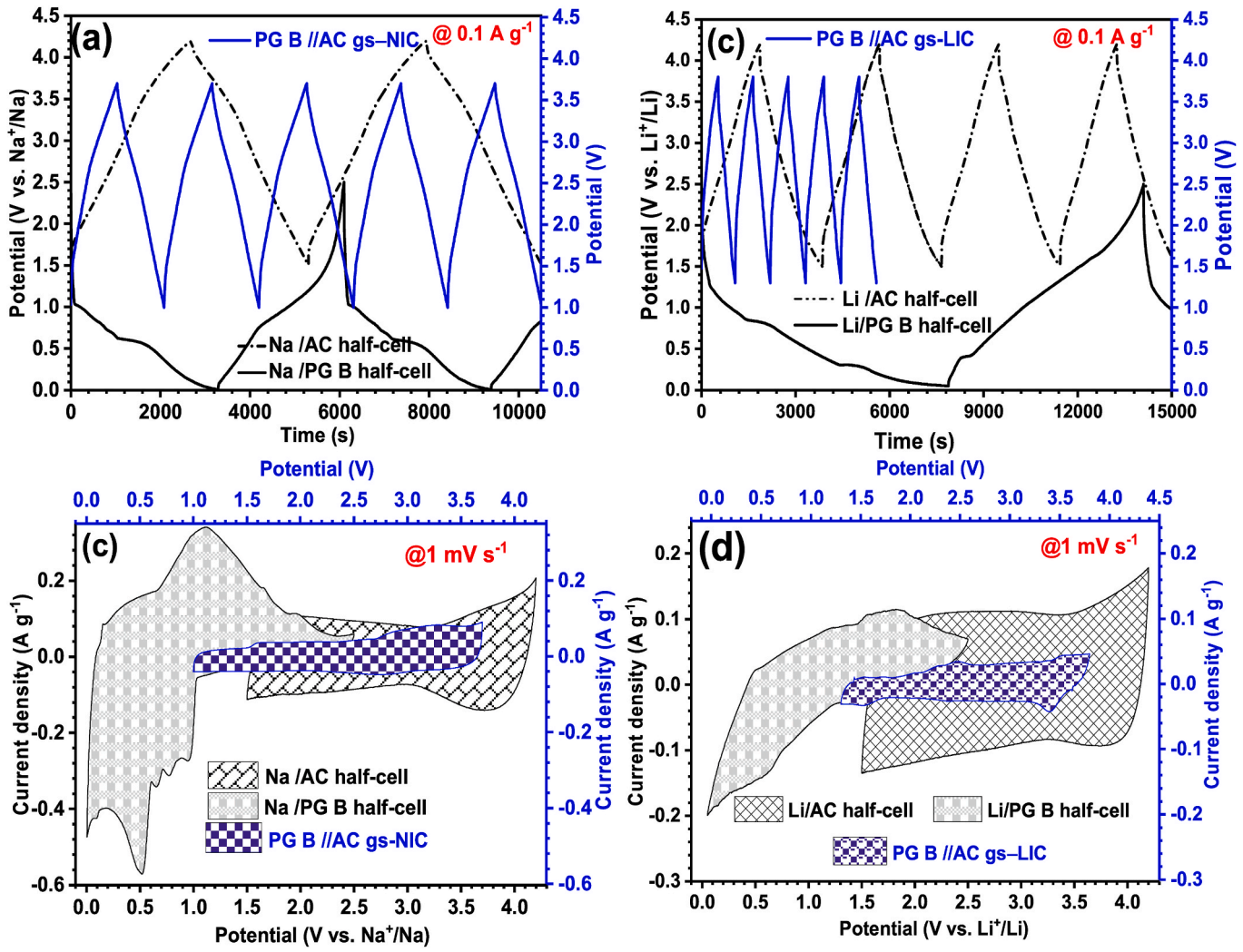

Fig. 5. Performance comparison of assembled AMIHSCs: (a) & (b) GCD profile of half-cells and co-intercalation based HSCs (PG B//AC gs−NIC and PG B//AC gs−LIC) at a current density of 0.1 A g^{-1}, and (c) & (d) CV profiles at a scan rate of 1 mV s^{-1}.

assembled gs-NIC over the gs-LIC device. Slow diffusion kinetics of G_4 solvated Li^+ ions over G_2 solvated Na^+ ions can be the main reason behind this performance disparity. Fig. 5(c& d) compares the CV profile of assembled glyme solvated NICs and LICs with their half-cell systems. Quasi rectangular shape CVs of the gs-NIC and gs-LIC show the presence of a hybrid charge storage mechanism (both capacitive and diffusion controlled). Table T1 illustrates the performance comparison of assembled glyme solvated AMIHSCs with previously reported works [24, 47–51]. It shows that the performance of PG B-based gs−NIC and gs−LIC are superior to or comparable with co-intercalation-based metal-ion capacitors containing other graphitic material anodes.

4. Conclusion

In summary, building high-performance AMIHSCs without/with minimum capacity and kinetic imbalance between the battery type and capacitive type electrodes is a real challenge, and it plays a vibrant role in the progress of electrochemical energy storage systems. Using pencil graphite (PG B), a low-cost and readily available graphitic material with silica content, as battery-type anode active material, and commercially available AC as active cathode material in the presence of glyme-based electrolytes (G_2 & G_4), we designed co-intercalation based hybrid capacitors (gs-NIC & gs-LIC). The PG B//AC gs−NIC and PG B//AC gs−LIC exhibited a maximum energy density of 78.7 Wh kg^{-1} (@ 125 W kg^{-1}) and 47 Wh kg^{-1} (@ 136 W kg^{-1}), respectively. The gs−NIC device prototype with a negligible imbalance in capacity and kinetics of electrodes exhibited excellent cyclic stability of ~97% capacity retention after 6000 charge-discharge cycles at a current density of 1 A g^{-1}. In comparison, the gs-LIC system could also retain 97% of its initial capacity after 3000 charge-discharge cycles at a current density of 1 A g^{-1}. Thus, the proposed co-intercalation-based AMIHSCs, mainly gs−NIC with PG B anode, is an excellent low-cost, high-performance (moderate energy-power storage capability with excellent cyclic stability) energy storage system that can manage to stand out among superior co-intercalation based configurations. However, there is still much more to do to achieve an ideal configuration with energy, power, and cycle life balanced performance, thus further exploring the electrochemical energy storage systems.

Conflicts of interest

There are no conflicts to declare.

CRediT authorship contribution statement

Madhusoodhanan Lathika Divya: by, Conceptualization, and, Formal analysis, Validation, Writing – original draft, Writing – review & editing, by. **Yun-Sung Lee:** Formal analysis, Validation, Writing –

original draft, Writing – review & editing, by. **Vanchiappan Aravindan:** Conceptualization, Formal analysis, Validation, Writing – original draft, Writing – review & editing, by, and.

Declaration of competing interest

The authors declare that they have no known competing financial interests or personal relationships that could have appeared to influence the work reported in this paper.

Data availability

Data will be made available on request.

Acknowledgments

MLD wishes to thank the funding through Women Scientist Scheme-B (DST/WOS-B/2018/2039) from the KIRAN division of the Department of Science & Technology (DST), Govt. of India. Y.S.L acknowledges the financial support from the National Research Foundation of Korea (NRF) grant funded by the Korean government (Ministry of Science, ICT& Future Planning) (No. 2019R1-A2C1007620). V.A. acknowledges financial support from the Science and Engineering Research Board (SERB), a statutory body of DST, Govt. of India, through Swarnajayanti Fellowship (SB/SJF/2020–21/12).

Appendix A. Supplementary data

Supplementary data to this article can be found online at https://doi.org/10.1016/j.jpowsour.2022.231823.

References

[1] L. Xia, B. Tang, J. Wei, Z. Zhou, Batteries & Supercaps 4 (2021) 1108–1121.
[2] J. Ding, W. Hu, E. Paek, D. Mitlin, Chem. Rev. 118 (2018) 6457–6498.
[3] P. Naskar, D. Kundu, A. Maiti, P. Chakraborty, B. Biswas, A. Banerjee, Chemelectrochem 8 (2021) 1393–1429.
[4] H. Wang, C. Zhu, D. Chao, Q. Yan, H.J. Fan, Adv. Mater. 29 (2017), 1702093.
[5] M. Iqbal, U. Aziz, J. Energy Storage 46 (2022), 103823.
[6] D.P. Chatterjee, A.K. Nandi, J. Mater. Chem. 9 (2021) 15880–15918.
[7] J. Liu, J. Wang, C. Xu, H. Jiang, C. Li, L. Zhang, J. Lin, Z.X. Shen, Adv. Sci. 5 (2017), 1700322, 1700322.
[8] S. Kaipannan, S. Marappan, Sci. Rep. 9 (2019) 1104, 1104.
[9] J.J. Lamb, O.S. Burheim, Energies 14 (2021).
[10] R.C. Massé, C. Liu, Y. Li, L. Mai, G. Cao, Natl. Sci. Rev. 4 (2017) 26–53.
[11] V. Aravindan, J. Gnanaraj, Y.-S. Lee, S. Madhavi, Chem. Rev. 114 (2014) 11619–11635.
[12] P. Lokhande, U. Chavan, A. Pandey, Electrochemical Energy Reviews 3 (2019).
[13] B. Li, J. Zheng, H. Zhang, L. Jin, D. Yang, H. Lv, C. Shen, A. Shellikeri, Y. Zheng, R. Gong, J.P. Zheng, C. Zhang, Adv. Mater. 30 (2018), 1705670.
[14] B. Li, C. Xing, H. Zhang, L. Hu, J. Zhang, D. Jiang, P. Su, S. Zhang, Chem. Eng. J. 421 (2021), 127832.
[15] C. Zheng, Y. Wang, Z. Liu, T. Sun, N. Kim, J. Jeong, S.W. Cha, International Journal of Precision Engineering and Manufacturing-Green Technology 8 (2021) 1739–1754.
[16] S.R. Sivakkumar, A.G. Pandolfo, Electrochim. Acta 65 (2012) 280–287.
[17] M.L. Divya, S. Natarajan, Y.-S. Lee, V. Aravindan, J. Mater. Chem. 8 (2020) 4950–4959.
[18] H. Zhang, Y. Yang, D. Ren, L. Wang, X. He, Energy Storage Mater. 36 (2021) 147–170.
[19] J. Asenbauer, T. Eisenmann, M. Kuenzel, A. Kazzazi, Z. Chen, D. Bresser, Sustain. Energy Fuels 4 (2020) 5387–5416.
[20] H. Kim, J. Hong, G. Yoon, H. Kim, K.-Y. Park, M.-S. Park, W.-S. Yoon, K. Kang, Energy Environ. Sci. 8 (2015) 2963–2969.
[21] B. Jache, P. Adelhelm, Angew. Chem. 126 (2014).
[22] L. Seidl, N. Bucher, E. Chu, S. Hartung, S. Martens, O. Schneider, U. Stimming, Energy Environ. Sci. 10 (2017) 1631–1642.
[23] M.L. Divya, Y.-S. Lee, V. Aravindan, ACS Energy Lett. 6 (2021) 4228–4244.
[24] M.L. Divya, S. Natarajan, Y.-S. Lee, V. Aravindan, ChemSusChem 13 (2020) 5654–5663.
[25] J. Park, Z.-L. Xu, K. Kang, Front. Chem. (2020) 432.
[26] S. Mamidi, A.K. Pandey, A.D. Pathak, T.N. Rao, C.S. Sharma, J. Alloys Compd. 872 (2021), 159719.
[27] H.-Y. Park, M.-S. Kim, T.-S. Bae, J. Yuan, J.-S. Yu, Langmuir 32 (2016) 4415–4423.
[28] Z. Tai, Y. Liu, Q. Zhang, T. Zhou, Z. Guo, H.K. Liu, S.X. Dou, Green Energy & Environment 2 (2017) 278–284.
[29] F. Tuinstra, J.L. Koenig, J. Chem. Phys. 53 (1970) 1126–1130.
[30] A. Ferrari, J. Robertson, S. Reich, C. Thomsen, Philos. Trans. R. Soc. London, Ser. A: Math. Phys. Eng. Sci. 362 (2004) 2271–2288.
[31] L. Bokobza, J.-L. Bruneel, M. Couzi, Chimia (2015) 1.
[32] Y. Wang, D.C. Alsmeyer, R.L. McCreery, Chem. Mater. 2 (1990) 557–563.
[33] R. Navratil, A. Kotzianova, V. Halouzka, T. Opletal, I. Triskova, L. Trnkova, J. Hrbac, J. Electroanal. Chem. 783 (2016) 152–160.
[34] A. Knápek, D. Sobola, D. Burda, A. Daňhel, M. Mousa, V. Kolařík, Nanomaterials 9 (2019).
[35] R. Mulla, D.R. Jones, C.W. Dunnill, Advanced Materials Technologies 5 (2020), 2000227.
[36] J. Landoulsi, M.J. Genet, S. Fleith, Y. Touré, I. Liascukiene, C. Méthivier, P. G. Rouxhet, Appl. Surf. Sci. 383 (2016) 71–83.
[37] B. Jache, J. Binder, T. Abe, P. Adelhelm, Phys. Chem. Chem. Phys. 18 (2016).
[38] M. Goktas, C. Bolli, J. Buchheim, E.J. Berg, P. Novák, F. Bonilla, T. Rojo, S. Komaba, K. Kubota, P. Adelhelm, ACS Appl. Mater. Interfaces 11 (2019) 32844–32855.
[39] Z.-L. Xu, G. Yoon, K.-Y. Park, H. Park, O. Tamwattana, S. Joo Kim, W.M. Seong, K. Kang, Nat. Commun. 10 (2019) 2598.
[40] Z.-L. Xu, J. Park, G. Yoon, H. Kim, K. Kang, Small Methods 3 (2019), 1800227.
[41] M.L. Divya, S. Jayaraman, Y.-S. Lee, V. Aravindan, Chem. Eng. J. 426 (2021), 130892.
[42] Y. Li, Y. Lu, P. Adelhelm, M. Titirici, Y.-S. Hu, Chem. Soc. Rev. 48 (2019).
[43] H.-L. Girard, H. Wang, A. d'Entremont, L. Pilon, J. Phys. Chem. C 119 (2015) 11349–11361.
[44] M. Goktas, C. Bolli, E.J. Berg, P. Novák, K. Pollok, F. Langenhorst, M.v. Roeder, O. Lenchuk, D. Mollenhauer, P. Adelhelm, Adv. Energy Mater. 8 (2018), 1702724.
[45] D. Aurbach, Y. Talyosef, B. Markovsky, E. Markevich, E. Zinigrad, L. Asraf, J. Gnanaraj, H.-J. Kim, Electrochim. Acta 50 (2004) 247–254.
[46] D. Morales, R.E. Ruther, J. Nanda, S. Greenbaum, Electrochim. Acta 304 (2019) 239–245.
[47] P. Han, X. Han, J. Yao, L. Zhang, X. Cao, C. Huang, G. Cui, J. Power Sources 297 (2015) 457–463.
[48] M.L. Divya, Y.-S. Lee, V. Aravindan, Batteries & Supercaps 4 (2021) 671–679.
[49] T. Huang, Z. Liu, F. Yu, F. Wang, D. Li, L. Fu, Y. Chen, H. Wang, Q. Xie, S. Yao, Y. Wu, ACS Appl. Mater. Interfaces 12 (2020) 52635–52642.
[50] T. Palaniselvam, B. Babu, H. Moon, I. Hasa, A.L. Santhosha, M. Goktas, Y.-N. Sun, L. Zhao, B.-H. Han, S. Passerini, A. Balducci, P. Adelhelm, Batteries & Supercaps 4 (2021) 173–182.
[51] X. Liu, G.A. Elia, B. Qin, H. Zhang, P. Ruschhaupt, S. Fang, A. Varzi, S. Passerini, ACS Energy Lett. 4 (2019) 2675–2682.